# Modeling Internal Energy Distributions in Ion Clusters: Comparison between Experiment and Simulations

**Orlando M. Cabarcos, Corey J. Weinheimer, and James M. Lisy***

*Department of Chemistry, University of Illinois at Urbana-Champaign, Urbana, Illinois 61801*

*Received: July 23, 1999; In Final Form: September 10, 1999*

The internal energy distribution of $Na^+(CH_3OH)_{1-8}$ cluster ions has been evaluated by comparing experimental unimolecular rate constants measured in a triple quadrupole spectrometer to an RRKM rate analysis developed within the evaporative ensemble formalism. The significant ion−solvent binding energies give rise to broad distributions, particularly for the smallest cluster ions. The role of internal energy on the number and type of cluster ion structures was then assessed by using Monte Carlo simulation methods. Predicted onsets of hydrogen bond formation and the number of hydrogen-bonded O−H stretching bands in $Na^+(CH_3OH)_{1-7}$ were found to agree with previous vibrational spectroscopy experiments. The methodology introduced here can be used to estimate the internal energy content of any cluster that undergoes unimolecular dissociation utilizing experimental or theoretical values for properties such as binding energies and vibrational frequencies.

## I. Introduction

From isolated species to nanoscale models of the condensed phase, the study of clusters is an interesting and challenging area of physical chemistry.[1−3] By means of mass-selective techniques, cluster systems are ideally suited for probing the stepwise evolution of molecular properties as a function of size and composition. Cluster size discrimination is most readily accomplished for ionic clusters, where the charge/mass ratio provides an efficient means of mass selection. In addition, the strong electrostatic interaction between the ion and neutral species leads to relatively stable and robust complexes. This allows for an extremely wide temporal window for investigation with time scales ranging from the picosecond[4] to the tens of seconds.[5−10]

The strong ion−solvent interaction also enables the clusters to retain a significant amount of internal energy without extensive fragmentation even under isolated conditions.[11−13] These large amounts of internal energy can lead to a number of complications in cluster ion experiments not usually shared with their neutral cluster counterparts. In systems that exhibit hydrogen bonding, there is a size where the ion−molecule and molecule−molecule interactions are of comparable magnitude. A broad internal energy distribution can therefore lead to structural isomers. This effect has been observed in previous studies of solvated alkali ions.[11,14,15]

The effects of cluster ion internal energy on vibrational spectroscopy are perhaps best illustrated in the recently published spectra of $X^-(H_2O)_1$ (X = Cl,[16] Br and I[17]). The most prominent bands in the O−H stretching region were assigned to the ionic O−H stretch, i.e., the $X^-\cdots H-O$ modes, under the assumption of low internal energy content. However, subsequent experiments[18,19] on similar cluster ions of the form $X^-(H_2O)_1Ar_n$, which take advantage of the extremely labile argon atoms to generate colder clusters, have revealed that the non-argon bearing species[16,17] contained substantial internal energy. The temperature dependence in $Cl^-(H_2O)_2$ has been simulated recently using a parametrized intermolecular potential.[20] As a result, a change was made in the vibrational assignment of the "ionic" hydrogen bond O−H stretch in the cases of $Cl^-$ and $Br^-$. High-resolution spectroscopy of "cold" cluster ions has been limited to a few systems. Rotationally resolved infrared spectra of $Rg-HCO^+$ (ref 21), $-HN_2^+$ (refs 22 and 23), $-CH_3^+$ (ref 24), and $-NH_4^+$ (ref 25) cluster ions have been obtained by Maier and Dopfer et al., while the $M^+-L$ electronic spectra [M = Ca, Mg, Ba; L = $H_2O$, Ar, $CO_2$, $C_2H_2$] have been recorded by Duncan and co-workers.[3,26−28] These high-resolution studies, however, have been restricted to only binary complexes and similar studies of larger cluster ions remain an open challenge.

The purpose of the present work is to provide a methodology for assessing the internal energy distribution in cluster ions and to compare the results from this analysis with experimental data, namely average unimolecular dissociation rates. Since many of these species can be generated by various methods such as electric discharge, ion injection, laser vaporization, and electron impact ionization, a common method for the determination of cluster ion energy content would be desirable. The internal energy distribution can then be used with simulation methods, such as Monte Carlo, molecular dynamics, or more sophisticated ab initio treatments, to predict possible molecular structures and their distributions. These, in turn, can be compared with experimental spectroscopic information or ab initio calculations at one or more minima on the potential energy surface.

The specific system selected for this comparison is $Na^+(CH_3OH)_{1-8}$. Previously, we have reported the vibrational spectra in the C−O (ref 29) and O−H (ref 30) stretching regions, noting the size of the first solvent shell, the onset of hydrogen bonding, and the presence of structural isomers. Using a three-site pairwise additive intermolecular force model, Monte Carlo simulations were used to estimate the solvent shell size and the onset of hydrogen bonding.[29] In this work, experimental unimolecular dissociation rates were determined from spontaneous solvent evaporation as a function of cluster size. Calculated unimolecular dissociation rates were determined from the internal energy distributions, by means of the evaporative ensemble,[31−33] experimental binding energies, and RRKM unimolecular rate theory. The temperatures derived from the internal energy distribution were used as input to *new* Monte Carlo simulations,

* Corresponding author. E-mail: j-lisy@uiuc.edu.

10.1021/jp9925637 CCC: $18.00 
Published on Web 10/21/1999

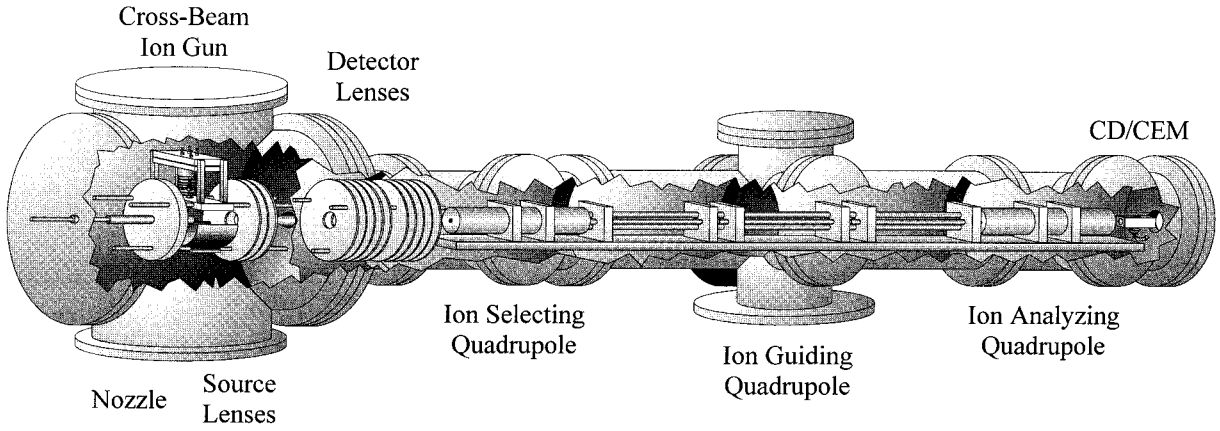


**Figure 1.** Schematic of the triple quadrupole mass spectrometer depicting both the source chamber, where ion clusters are formed, and the detector chamber, where ion clusters are analyzed.

using a fully polarizable potential to evaluate $Na^+(CH_3OH)_{1-8}$ cluster ion structures. On the basis of the more accurate internal energies and improved potential model, structural features of the infrared spectra of $Na^+(CH_3OH)_{1-7}$ are re-examined.

## II. Experimental Section

**A. Apparatus.** The experimental apparatus used for these studies has been discussed in previous publications.[14,30,34,35] Briefly, it consists of two differentially pumped chambers separated by an interchamber skimmer (Figure 1). The nozzle, skimmer, and quadrupole axes are collinear. Sodium ions are produced in the source chamber by thermionic emission from a coated filament in an ion gun,[36] mounted perpendicular to the molecular beam axis. Alumina treated with aqueous saturated NaCl is applied to the filament prior to use. The emitted ions are focused into a fully expanded supersonic jet generated by expanding methanol in argon (1:5 ratio) through a 45°, 180 $\mu$m diameter conical nozzle at a stagnation pressure of 300 Torr. Cluster ions are formed by the resulting collision and extracted into the detector chamber with the aid of electrostatic lenses and the interchamber skimmer (1 mm diameter). During this transport process of 50−100 $\mu$s, the nascent cluster ion distribution has undergone a series of evaporative events to dissipate the excess internal energy resulting from the initial collision and the subsequent exothermic solvation processes. The cluster ions are then imaged by a second set of electrostatic lenses into a series of three quadrupoles, the first of which is used to mass-select the cluster ion of interest. The cluster ions enter a second quadrupole (RF-only guide) where they continue to undergo unimolecular dissociation and, in addition, vibrational excitation using a tunable IR laser or collision-induced dissociation (CID) by collision with a background gas. The resulting increase in the internal energy of the cluster ion from the latter two processes leads to a detectable increase in the dissociation rate during the transit time (∼100−300 $\mu$s) through the second quadrupole. The ensemble of cluster ions then passes into the third and final mass analyzing quadrupole at which point the parent and daughter ion distributions are determined.

**B. Collision Induced Dissociation Experiments.** For cluster ions undergoing evaporative cooling, the spontaneous unimolecular dissociation of the cluster ion will involve loss of the most labile molecule. Abrupt changes in the rate of unimolecular dissociation at a particular cluster size can be indicative of a significant alteration in the structure of the cluster ion, such as the filling of a solvent shell. However, at ambient pressures in the detector chamber, collision-induced dissociation can also occur. To differentiate between the two processes, the fragmentation of a specific cluster ion is measured at various detector chamber pressures. The pressure is controlled by introducing argon as a collision gas into the detector chamber through a leak valve. Extrapolating to zero pressure yields the extent of fragmentation in the absence of collisions, i.e., the spontaneous dissociation of the size-selected cluster ion. The fragmentation patterns were recorded over a range of $1.0 \times 10^{-6}$ to $3.0 \times 10^{-6}$ Torr, to ensure that single collision conditions were maintained. Additional details can be found elsewhere.[11]

The only unimolecular dissociation loss channel observed was the loss of one methanol solvent. The fractional depletion of the mass-selected cluster ion, $D = 1 - I_{f,1}/I_0$, was fit as a function of pressure, and the extrapolated value at zero pressure was taken as the fraction of the parent ion cluster that underwent unimolecular dissociation. $I_{f,n}$ is the intensity of the fragment ion corresponding to the loss of $n$ solvent molecules from the parent, and $I_0$ is the sum of the intensities of the parent ion and all the measured ion fragments. The extent of unimolecular dissociation was found to vary from less than 1% for $Na^+(CH_3OH)_2$ to ∼8% for $Na^+(CH_3OH)_8$. The reported average unimolecular dissociation rates, $\langle k \rangle$, in the ion guiding region for a particular loss channel were calculated by

$$\langle k \rangle = -\ln[D(P=0)]t^{-1} \quad (1)$$

where $t$ is the flight time of the ions through the middle quadrupole.

## III. Internal Energy Distributions

Internal energy distributions of the ion clusters in the experimental apparatus are modeled by (a) calculating the unimolecular dissociation rates for each cluster as a function of internal energy and (b) following the evolution of the cluster population using experimental flight times through the tandem mass spectrometer under the assumptions of the evaporative ensemble. Previous investigations in our laboratory on $Na^+(CH_3OH)_n$ relied on RRK theory to determine rates as a function of internal energy.[29] RRK rates, however, are based on a single average vibrational frequency and thus will yield unreliable estimates for the internal energy distribution. For this reason, the unimolecular dissociation rates of $Na^+(CH_3OH)_n$ have been calculated using the more rigorous RRKM theory.[37]

**A. RRKM Method.** The necessary vibrational frequencies of the cluster ion internal modes were obtained from HF ab initio calculations using a double-$\zeta$ basis set for $Na^+(CH_3OH)_{1-4}$. These frequencies were scaled by a factor of 0.9 to account for the difference between the harmonic calculations and the

**TABLE 1: Vibrational Frequencies of $Na^+(CH_3OH)_{1-9}$[a]**

| 1 | 2 | 3 | 4 | 5 | 6 | 7 | 8 | 9 |
|---|---|---|---|---|---|---|---|---|
| 3739 | 3743 (2) | 3752 (3) | 3759 (4) | 3759 (5) | 3759 (6) | 3759 (7) | 3759 (8) | 3759 (9) |
| 2981 (2) | 2981 (2) | 2976 (3) | 2977 (4) | 2977 (5) | 2977 (6) | 2977 (7) | 2977 (8) | 2977 (9) |
| 2897 | 2972 (2) | 2962 (3) | 2951 (4) | 2951 (5) | 2951 (6) | 2951 (7) | 2951 (8) | 2951 (9) |
| 1477 | 2894 (2) | 2889 (3) | 2884 (4) | 2884 (5) | 2884 (6) | 2884 (7) | 2884 (8) | 2884 (9) |
| 1460 (2) | 1477 (2) | 1478 (3) | 1478 (4) | 1478 (5) | 1478 (6) | 1478 (7) | 1478 (8) | 1478 (9) |
| 1355 | 1462 (2) | 1464 (3) | 1466 (4) | 1466 (5) | 1466 (6) | 1466 (7) | 1466 (8) | 1466 (9) |
| 1150 | 1459 (2) | 1460 (3) | 1458 (4) | 1458 (5) | 1458 (6) | 1458 (7) | 1458 (8) | 1458 (9) |
| 1068 | 1355 (2) | 1352 (3) | 1348 (4) | 1348 (5) | 1348 (6) | 1348 (7) | 1348 (8) | 1348 (9) |
| 989 | 1151 (2) | 1152 (3) | 1154 (4) | 1154 (5) | 1154 (6) | 1154 (7) | 1154 (8) | 1154 (9) |
| 288 | 1066 (2) | 1063 (3) | 1058 (4) | 1058 (5) | 1058 (6) | 1058 (7) | 1058 (8) | 1058 (9) |
| **408** | 1000 | 1014 | 1025 | 1021 (5) | 1021 (6) | 1021 (7) | 1021 (8) | 1021 (9) |
| **136** | 997 | 1009 (2) | 1020 (3) | 379 (4) | 379 (5) | 379 (5) | 379 (6) | 379 (6) |
| **95** | 401 | 391 (2) | 395 | 232 (5) | 232 (6) | 232 (7) | 232 (8) | 232 (9) |
| | 324 | 278 (2) | 377 | 130 (3) | 130 (3) | 130 (3) | 130 (3) | 130 (3) |
| | 210 | 201 | 358 | 104 (2) | 104 (4) | 104 (6) | 104 (8) | 104 (10) |
| | 146 | 127 | 251 | 93 (3) | 93 (3) | 93 (3) | 93 (3) | 93 (3) |
| | 95 | 117 | 247 | 60 (3) | 60 (4) | 60 (5) | 60 (6) | 60 (7) |
| | **394** | 93 | 244 | 30 (2) | 30 (3) | 100 | 100 | 100 (2) |
| | **102** | 90 | 188 | 22 | 22 | 30 (4) | 30 (5) | 30 (6) |
| | **89** | 43 | 137 | 15 (2) | 15 (3) | 22 | 22 | 22 |
| | **41** | 16 | 122 | 9 | 9 | 15 (4) | 15 (5) | 15 (6) |
| | **23** | 14 | 114 | **100** | **100** | 9 | 9 | 9 |
| | **18** | **389** | 102 | **104 (2)** | **104 (2)** | **100** | **100** | **100** |
| | | **126** | 91 (2) | **60** | **60** | **104 (2)** | **104 (2)** | **104 (2)** |
| | | **91** | 50 (2) | **30** | **30** | **60** | **60** | **60** |
| | | **51** | 35 | **15** | **15** | **30** | **30** | **30** |
| | | **42** | 15 | | | **15** | **15** | **15** |
| | | **9** | 14 | | | | | |
| | | | 9 | | | | | |
| | | | **384** | | | | | |
| | | | **104 (2)** | | | | | |
| | | | **60** | | | | | |
| | | | **31** | | | | | |
| | | | **22** | | | | | |

[a] The numbers in parentheses are the degeneracies for a given mode. The frequencies listed in bold are lost upon evaporation of the solvent. The first frequency listed in bold for a particular cluster size is the transition state frequency and is removed when the sums of states of the transition complex are calculated.

observed intramolecular frequencies of methanol monomer[38] (Table 1). The frequencies for the larger clusters, $Na^+(CH_3OH)_{5-9}$, were assigned based on trends in the smaller clusters. Also necessary are the degeneracy ($d$) and frequency of the normal mode along the reaction coordinate that leads to the dissociative transition state. For the smaller ion clusters, $Na^+(CH_3OH)_{1-4}$, these "transition state frequencies" were chosen as the ion−solvent stretching frequencies, which range from 384 to 408 $cm^{-1}$. The degeneracy factor was taken to be the number of solvent molecules in the ion cluster ($d = n$).

For the larger clusters, $n = 5-9$, the vibrational predissociation spectra[30] of $Na^+(CH_3OH)_n$ and preliminary Monte Carlo simulations indicate population of the second solvent shell. These molecules are expected to have a lower binding energy than those in the first shell and a value of 100 $cm^{-1}$ was assumed for the transition state frequency. Since these very molecules are expected to be the most labile, the degeneracy was likewise taken to be the average number of solvent molecules present in the second solvation shell for $n = 5-9$. On the basis of the preliminary Monte Carlo simulations, the number of solvent molecules in the second solvation shell was determined to be one for $n = 5$, 6; two for $n = 7$, 8; and three for $n = 9$.

The last required data are the solvent binding energies, which determine the minimum amount of energy required to reach the transition state. The binding energies for $n = 1-4$ have been determined experimentally by Castleman.[39] For the larger cluster ions, where solvent loss is expected to originate from the second solvation shell, the bulk solvent binding energy for methanol was used. Table 2 summarizes the data used in the calculations.

**TABLE 2: Binding Energies, Average Internal Energies, Temperatures, and MC Temperatures (Calculated RRKM Temperatures of the Cluster Ion Distributions and the Corresponding Temperature at Which the MC Simulations Were Performed)**

| n | $E_{binding}$ (kJ/mol) | average internal energy (kJ/mol)[a] | average temperature (K)[a] | Monte Carlo run (K) |
|---|---|---|---|---|
| 1 | 110.3[b] | 56 (6) | 890 (60) | 650[d] |
| 2 | 87.2[b] | 52 (8) | 510 (40) | 500 |
| 3 | 75.6[b] | 56 (10) | 400 (40) | 400 |
| 4 | 68.3[b] | 61 (11) | 340 (30) | 350 |
| 5 | 48.5[c] | 58 (12) | 280 (30) | 275 |
| 6 | 48.5[c] | 68 (14) | 270 (30) | 275 |
| 7 | 48.5[c] | 77 (16) | 260 (30) | 250 |
| 8 | 48.5[c] | 87 (18) | 260 (30) | 250 |

[a] Errors were determined by adding the error resulting from changing the binding energies by ±10% and the intermolecular vibrational frequencies by ±25% independently. [b] Binding energies were calculated from enthalpies of association obtained by high-pressure mass spectrometry.[39,66] [c] Determined from the bulk phase enthalpy of vaporization for methanol.[67] [d] This was the highest temperature at which the simulation did not experience solvent "walk-off".

The RRKM dissociation rate, $k$, as a function of vibrational internal energy, $E_v$, is given by the following formula:[40]

$$k(E_v) = \left(\frac{Q^{\ddagger}}{Q}\right)\frac{dW_v^{\ddagger}(E_v - E_B)}{hN_v(E_v)} \qquad (2)$$

where $E_B$ is the binding energy of the solvent dissociating from the cluster, $N_v$ is the vibrational density of states of the cluster,

$W_v^{\ddagger}$ is the vibrational sum of states of the transition state complex, $h$ is Planck's constant, and $Q^{\ddagger}/Q$ is the ratio of the rotational partition functions of the transition state to the energized molecule. The sums of states for both the energized and transition state complexes were calculated using the Beyer−Swinehart algorithm.[41,42] For the energized complex, all vibrational frequencies were included in the sum of states calculation, whereas for the transition state complex, the frequency associated with the normal mode along the reaction coordinate was removed. The density of states of the transition state complex was calculated using the finite difference method.

Our approach to the dissociation of cluster ions closely follows that of Armentrout and co-workers.[43−45] Here, the height of the centrifugal barrier is half of the rotational energy at the transition state. Assuming that the 2-D rotational energy is given by $k_bT$, the ratio of the moments of inertia and thus the rotational partition functions ($Q^{\ddagger}/Q$) was determined using the following relationship:

$$\frac{Q^{\ddagger}}{Q} = \frac{I^{\ddagger}}{I} = \left(\frac{\alpha e^2}{8\epsilon_0 r_e^4 k_b T}\right)^{1/2} \tag{3}$$

where $r_e$ is the center of mass equilibrium distance between the dissociating molecule and the remaining ion fragment, $\alpha$ is the polarizability of methanol, $e$ is the elementary charge constant, $\epsilon_0$ is the vacuum permittivity constant, $k_b$ is the Boltzmann constant, and $T$ is the temperature of the cluster. For the $Na^+(CH_3OH)_n$ system, minima in the ion-methanol radial distribution functions from Monte Carlo simulations were chosen for the barrier points, with $r_e$ taken as 2.5 Å for first shell solvent molecules and 5.0 Å for second shell solvent molecules.

Since an evaporative process is being modeled, the remaining internal energy is distributed into products. The portion released as kinetic energy is taken as $2k_bT^{\ddagger}$.[33,46] The remaining energy in the dissociation products is statistically distributed among the available vibrational and rotational degrees of freedom of the product species.

**B. Evaporative Ensemble.** As in our previous work, the evaporative ensemble formalism[31−33] was used in the equations governing the evolution of the cluster ion populations. The RRKM rates, determined above, were used to simulate the propagation of an ion distribution through the experimental apparatus.[47] The simulations were simplified by considering the internal energy distributions of only three cluster ions; the parent cluster ion of interest, $n$, and the corresponding grandparent and fragment cluster ions, $n + 1$ and $n - 1$. A flat distribution was assumed for the $n + 1$ cluster ion at the source since the velocity spread of the impacting ion and the distribution of neutral solvent clusters in the expansion are expected to lead to a broad initial spread in the cluster ion internal energy. The distributions of both the $n$ and $n - 1$ ion clusters were initially set to zero following one of the tenets of the evaporative ensemble formalism, which assumes that at least one evaporative event occurs prior to the detection of the ion distributions. The $n + 1$ and $n$ cluster ion distributions were followed for the period of time needed to reach the entrance of the first quadrupole. At this point, the $n + 1$ cluster ion distribution was eliminated, while the $n$ cluster ion was allowed to continue decaying, in effect modeling the passage of the ion clusters through the quadrupole filter tuned to the mass of the parent cluster ion. After entering the middle or ion guiding region, the $n$ and $n - 1$ cluster ion distributions were allowed to evolve over the flight time needed to traverse this portion of the apparatus. All cluster ion transit times used in these calculations correspond to actual experimental flight times measured in the apparatus.[11] The final $n$ and $n - 1$ cluster ion distributions exiting the third quadrupole were used to calculate the relative fragmentation, $F(t)$, using

$$F(t) = \frac{\int P_{n-1}(E,t)\,dE}{\int P_{n-1}(E,t)\,dE + \int P_n(E,t)\,dE} \tag{4}$$

where $P_{n-1}(E,t)$ and $P_n(E,t)$ are the respective population distributions of the parent and fragment clusters ions as a function of internal energy $E$ at time $t$.[47] Note that the evolution of the $n$ and $n - 1$ distributions mimics the experimental distributions in the absence of collision-induced dissociation. The average unimolecular dissociation rate, $\langle k \rangle$, is then calculated by

$$\langle k \rangle = -\ln(1 - F(t'))/t' \tag{5}$$

where $t'$ is the average flight time of the cluster ions of size $n$ through the ion guiding region of the mass spectrometer where product ions are formed. These average rates can be directly compared with experimentally measured values obtained using eq 1.

The internal energy distributions and the vibrational frequencies from the RRKM rate calculations can also be used to estimate temperatures for the cluster ions. The relationship between temperature and total internal energy is given below.

$$\mathrm{IE_{vr}}(T) = \sum_{j=1}^{m} E_{vj}(T) + \mathrm{IE_r}(T) \tag{6}$$

$$\mathrm{IE_r}(T) = \frac{3}{2}k_bT \tag{7}$$

$$E_{vj} = \frac{k_b\Theta_{vj}\, e^{\Theta_{vj}/T}}{(1 - e^{\Theta_{vj}/T})} \quad \text{with} \quad \Theta_{vj} = \frac{h\nu_j}{k_b} \tag{8}$$

where $\mathrm{IE_{vr}}(T)$ is the total internal energy (rotation + vibration), $E_{vj}$ is the internal energy contribution of the $j$th vibrational mode of the cluster, $m$ is the total number of vibrational modes in the cluster, $\mathrm{IE_r}$ is the rotational energy component to internal energy, $T$ is the rotational−vibrational temperature, and $\nu_j$ is the frequency of the $j$th vibrational mode. Temperatures of the ion cluster distributions are calculated at the entrance and exit of the middle ion-guiding region and then averaged to estimate a temperature for each ion cluster.

Equations 6−8 are also used to partition the internal energy between the vibrational and rotational degrees of freedom. In this manner, the rotational contribution to temperature is taken into account. These equations are also used to calculate the temperature of the transition state, $T^{\ddagger}$, using the appropriate frequencies and $E - E_{\mathrm{binding}}$ as the available energy at the transition state. The $T^{\ddagger}$ is important for determining the amount of relative kinetic energy released upon evaporation of a solvent molecule as discussed previously.

## IV. Monte Carlo Simulations

**A. Methods.** Metropolis Monte Carlo (MC) simulations[48−50] are used to probe the structure of $Na^+(CH_3OH)_n$ ion clusters. The MC simulations proceed in two stages for each cluster size simulated. The first stage is an annealing process that generates equilibrated ion cluster configurations at various temperatures. The starting temperature is taken to be at least 25 K higher than any temperature of potential interest. The simulations begin

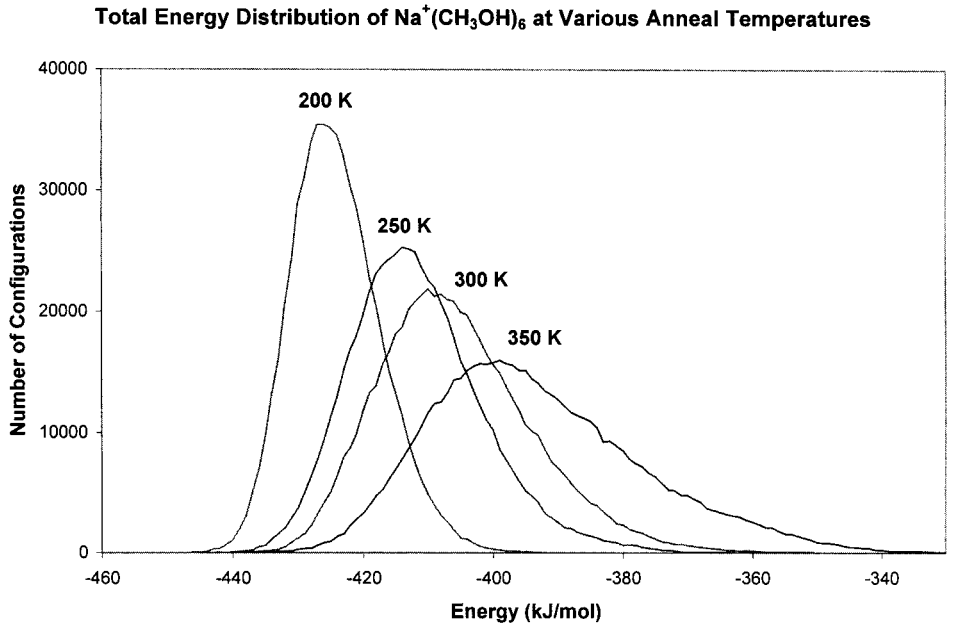


**Figure 2.** Plot showing the total energy distribution dependence with temperature. The average total energy of the cluster is $-393 \pm 17$ kJ/mol at 350 K and lowers to $-424 \pm 7$ kJ/mol at 200 K.

by randomly placing the methanol molecules in a box that contains the $Na^+$ ion at the center, and whose size is chosen to yield the number density of liquid methanol at an arbitrarily chosen temperature of 293 K. For each MC iteration, a randomly chosen methanol molecule is rotated and translated randomly in three dimensions. After 100 000 iterations per solvent, the temperature of the system is lowered by 25 K and the Metropolis sampling is repeated until the desired final temperature is reached. The average and the standard deviation of the ion−solvent, solvent−solvent, polarization, and total energy are calculated and stored at each temperature, as is the final structural configuration of the system. A sample of the total energy distribution for $Na^+(CH_3OH)_6$ at several anneal temperatures is presented in Figure 2, graphically displaying the expected trend to narrower distributions at lower energy. The second stage of the simulations involves a more detailed statistical analysis at a *single* temperature, which calculates many different system properties for a more complete characterization of the cluster ion system based on 1 000 000 iterations per solvent. Detailed aspects of the calculations are discussed further below. In both sets of simulations, a random move acceptance ratio between 30 and 50% is desirable[51] for the efficient sampling of phase space. Typical movement parameters used in the current MC simulations are ~0.15 Å for translation and 0.30 rad for rotation.

**B. Polarizable Potential Force Field.** An important distinction of these MC simulations from earlier work[29,51] is the use of a nonadditive all-atom potential force field, based on a model by Kollman et al.[52] All six atoms of the methanol molecule are explicitly included and are represented by the standard Lennard-Jones parameters, a partial charge and an isotropic atom polarizability.[53] The $Na^+$ ion is represented similarly. The total potential is given as

$$V_{\text{total}} = \sum_{i=1}^{N}\sum_{j>1}^{N} V(r_{ij}) = \sum_{i=1}^{N}\sum_{j>1}^{N}\left[4\epsilon_{ij}\left(\frac{\sigma_{ij}^{12}}{r_{ij}^{12}} - \frac{\sigma_{ij}^{6}}{r_{ij}^{6}}\right) + \frac{q_i q_j}{r_{ij}}\right] - \frac{1}{2}\sum_{i=1}^{N}(\vec{\mu}_i \cdot \vec{E}_i^0) \quad (9)$$

where $N$ is the total number of atoms, $r_{ij}$ is the distance between atom $i$ and atom $j$, and $q_i$ and $q_j$ are the respective partial charges. The Lennard-Jones parameters, $\epsilon_{ij}$ and $\sigma_{ij}$, are combined by taking the geometric and arithmetic average of the individual atom parameters, respectively. The first two terms in eq 9 represent the sum over the Lennard-Jones terms, the third is the electrostatic contribution and the last term represents the energy of polarization. In the polarization energy term, $\vec{\mu}_i$ is the induced dipole moment at atom $i$ and $\vec{E}_i^0$ is the static electric field at atom $i$ due to the partial charges on the other atoms. The induced dipole is calculated using

$$\vec{\mu}_i = \alpha_i \vec{E}_i \quad (10)$$

where $\alpha_i$ is the isotropic polarizability of atom $i$. The total electric field, $\vec{E}_i$ at the atom is given by

$$\vec{E}_i = \vec{E}_i^0 + \sum_{j=1, j\neq i}^{N} \tilde{T}_{ij}\vec{\mu}_j \quad (11)$$

where

$$\vec{E}_i^0 = \sum_{j=1, j\neq i}^{N} q_j \frac{\vec{r}_{ij}}{r_{ij}^3} \quad (12)$$

represents the static electric field contribution and

$$\tilde{T}_{ij} = \frac{1}{r_{ij}^3}\left(3\vec{r}_{ij}\left(\frac{\vec{r}_{ij}}{r_{ij}^2}\right) - 1\right) \quad (13)$$

represents the dipole tensor matrix elements. All of the summations are over nonbonded atoms with the exception of the polarization term where the interactions between the hydroxyl hydrogen and methyl hydrogens are included. The calculation of the electric fields is repeated until the results are self-consistent. Four iterations are typically required for convergence to one part in 1 million. The potential parameters are listed in Table 3.

**TABLE 3: Polarizable Potential Parameters Used in the Monte Carlo Simulations**

| atom | $q^c$ (e) | $\epsilon$ (kJ/mol) | $\sigma$ (Å) | $\alpha$ (Å$^3$) |
|---|---|---|---|---|
| | | Ion[a] | | |
| $Na^+$ | 1.000 | 0.5439 | 2.156 | 0.240 |
| | | Methanol[b] | | |
| hydroxyl H | 0.3281 | 0.0 | 0.0 | 0.135 |
| O | −0.5057 | 0.8803 | 3.0665 | 0.465 |
| C | 0.0908 | 0.4577 | 3.3997 | 0.878 |
| methyl H | 0.0290 | 0.0657 | 2.4714 | 0.135 |

[a] Reference 54. [b] Reference 52. [c] The partial charges for methanol were scaled by a factor of 0.78 from the original reference.

**TABLE 4: Methanol Geometry[a] Used in the Monte Carlo Simulations**

| bond lengths (Å) | bond angles (degrees) |
|---|---|
| $R_{O-H} = 0.960$[b] | ∠C−O−H = 108.0° |
| $R_{C-O} = 1.41$ | ∠H−C−H = 109.5° |
| $R_{C-H} = 1.098$ | ∠H−C−O = 109.5° |

[a] Reference 52. [b] Reference 68.

The original implementation of the polarizable methanol potential by Kollman[52] included additional bond, angle, and dihedral energy terms to model a flexible molecule for use in molecular dynamics simulations of liquid methanol. In our MC simulations, the methanols are modeled as rigid molecules at the gas-phase equilibrium geometry of methanol monomer. The fixed bond lengths and angles are given in Table 4. This geometry, with the original partial charges provided by Kollman, resulted in an abnormally large dipole moment of 2.17 D for methanol as compared to the experimentally measured value of 1.69 D. (This was not the case in the MD simulations by Kollman where the flexible methanol in an energy-minimized geometry was found to have a dipole moment of 1.90 D.) To correct for the rigid geometry used in the MC calculations, the partial charge distribution was scaled by a factor of 0.78 to yield the experimental dipole of 1.69 D. The parameters for $Na^+$ are also taken from Kollman[54] and are used without further modification.

To benchmark the modified methanol potential, MC simulations of the methanol dimer were performed at 1 K. This yielded a minimum dimer binding energy of 18.6 kJ/mol, which is reasonably close to the dimer binding energy of 17.2 kJ/mol determined from ab initio calculations by Mó et al.[55] and the experimentally measured value of 15 ± 3 kJ/mol.[56] The calculated O···H hydrogen bond distance of 1.90 Å is also in good agreement with the value of 1.96 Å determined by microwave spectroscopy.[57] Similar MC simulations of $Na^+$ with one methanol gave a binding energy of 105.3 kJ/mol, in close agreement with the experimentally measured binding energy of 108.8 kJ/mol.[58] A plot of the $Na^+$−methanol potential is given in Figure 3.

**C. Monte Carlo Analyses.** One of the primary incentives for performing the MC simulations is to gain insight into the structural configurations of the cluster ions accessible over the range of internal energies/temperatures present in our apparatus. One of the more useful diagnostic tools, is the pair radial distribution functions (RDF), representing the probability that an atom will be found in a spherical shell of thickness d$r$ at a distance $r$ away from a central site with respect to a homogeneous solution of density $\rho$. The RDFs are calculated using[50]

$$G(r) = \frac{N(r,s)}{V \cdot s \cdot \rho} \tag{14}$$

where $N(r,s)$ is the number of atoms observed in the shell, $s$ is the total number of iterations per solvent in the simulation, $\rho$ is equal to 1.0 (corresponding to a solution of unit density), and $V$ is the volume of the shell. Integrating $G(r)$ over all space yields the total number of atoms surrounding the site. The large electrostatic charge of the ion and its subsequent influence on cluster ion structure make it a natural choice for selection as a central site in the calculation of RDFs. Ion−solvent RDFs are calculated for the $Na^+$−O, $Na^+$−hydroxyl H, and the $Na^+$−C atom pairs. These RDFs yield structural information on the formation of solvent shells about the ion. By integrating over the resolved peaks in the RDFs, occupancy numbers for the different solvent shells can be obtained.

Intermolecular interactions between the solvent molecules are examined by analyzing the pairwise RDFs between atomic sites on each methanol molecule. Specifically, the methanol−

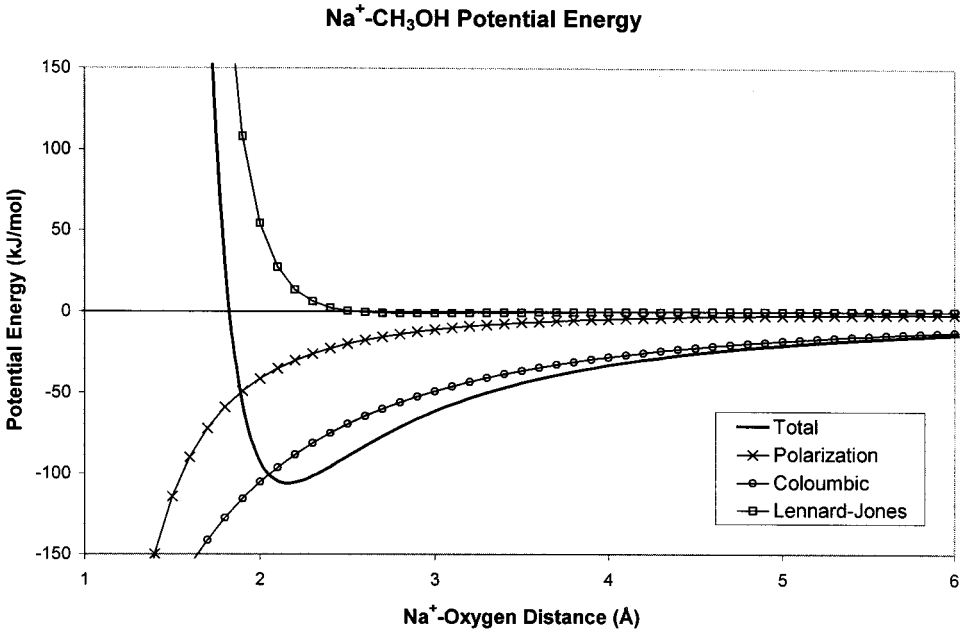


**Figure 3.** The sodium−methanol interaction potential. The potential is calculated with the ion in the plane formed by the methanol oxygen, carbon, and hydroxyl hydrogen. The oxygen is closest to the ion and the ion−oxygen−carbon angle is 104°.

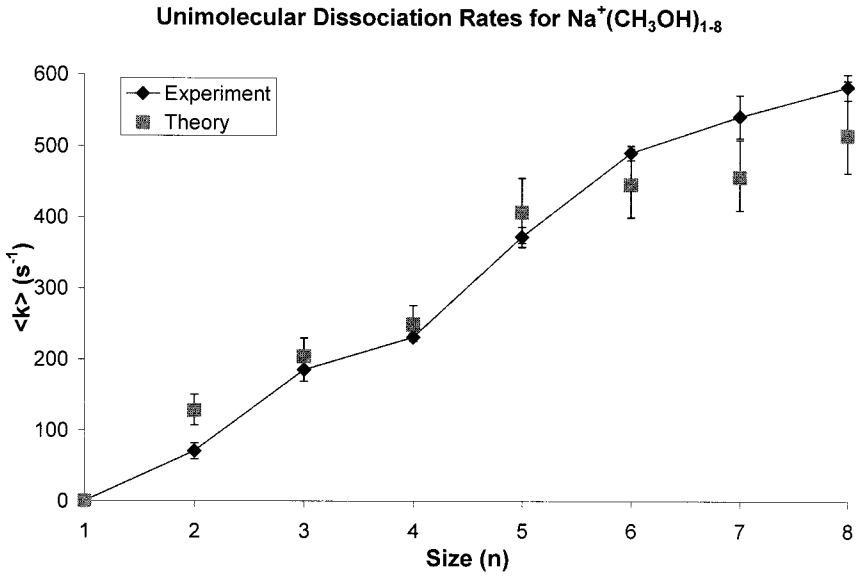


**Figure 4.** Experimental and calculated unimolecular dissociation rates of $Na^+(CH_3OH)_{1-8}$. The experimental error bars, representing two units of standard deviation, are taken as the sum of the error introduced by scaling all the intermolecular vibrational frequencies (soft modes) by ±25% and the binding energies by ±10%.

methanol RDFs between the O−O, O−hydroxyl H, and hydroxyl H−hydroxyl H atomic sites are calculated. The ion−solvent and solvent−solvent RDFs were examined from 0 to 20.0 Å at a resolution of 0.1 Å. This resolution was found more than sufficient to detail the solvent shell structure. The O−hydroxyl H RDF, in particular, can offer details on hydrogen bond formation. However, calculating the distance between the hydroxyl hydrogens and the oxygen atoms of different methanol pairs provides a more definitive measure of hydrogen bonding. Two molecules are considered to be hydrogen-bonded if the donor hydrogen atom and the acceptor oxygen atom are less than 2.5 Å apart and if the angle defined by the donor atom, hydrogen atom, and acceptor atom is between 145° and 180°.[29] The average number of hydrogen bonds formed, the average distance, and angle of formation, are also tabulated. Additionally, the percentage of MC iterations in which each solvent molecule acts as a hydrogen bond donor or acceptor throughout the simulation is determined since the information can be related to the solvent shell occupancy of each methanol molecule. For instance, if the solvent molecule has a preference toward acting as a proton donor, this can be correlated with the solvent being positioned in the first solvation shell. Conversely, a methanol acting as a proton acceptor would correlate with a position in the second solvent shell.

Angular distribution functions are computed to better understand the spatial arrangement of the methanols around the ion. The angle formed between the oxygen of one methanol, the ion and the oxygen of a second methanol, $\angle O_1-Na^+-O_2$, is calculated for all the possible methanol solvent pairs. The distribution provides a useful diagnostic for determining whether the solvent molecules are symmetrically or asymmetrically solvating the ion for cluster ions with no occupation of the second solvent shell.

Histograms of the ion−solvent, solvent−solvent, polarization, and total energy of the cluster ion system are calculated throughout the simulation. The distributions, their averages, and their standard deviations are determined at the end of the run. Similarly, energy histograms for each individual solvent are also tabulated throughout the simulation, with the averages and standard deviations summarized along with each solvent's average center of mass distance (COM). Structural aspects of the cluster are directly reflected in the energetics of the solvent molecules. For example, first shell solvent molecules tend to have positive solvent−solvent interaction energies due to steric repulsion. Upon formation of a hydrogen bond (typically with a solvent in the second solvation shell), the solvent−solvent interaction energy becomes favorable. Additional details of the various analyses may be found elsewhere.[36]

## V. Results and Discussion

**A. RRKM Analysis.** The ability to compare experimentally measured average unimolecular dissociation rates to RRKM/evaporative ensemble calculations offers the opportunity to establish the internal energy distribution for cluster ions generated under our exact experimental conditions. As can be seen in Figure 4, the agreement between the experimental and calculated values is quite good. The internal energy distributions from RRKM/EE calculations are shown in Figure 5, and the resulting cluster ion temperatures are given in Table 2. The binding energy of the solvent decreases with the addition of each methanol molecule, while the number of low-frequency intermolecular vibrational modes increases by six. This results in ion clusters with progressively narrower internal energy distributions. This is consistent with the observation by Klots[31−33] that the width of the internal energy distributions should be comparable to the binding energy of the fragment.

A representative temperature distribution is shown for $Na^+(CH_3OH)_5$ in Figure 6. The shape of this distribution is clearly non-Boltzmann, a result that is not unexpected. Since the ion clusters in the mass spectrometer exist in a vacuum, they can only dissipate energy radiatively or by undergoing unimolecular dissociation. The infrared radiative lifetimes of these energized clusters are long (∼10 ms) compared to the 100−300 $\mu$s time scale of the experiment, leaving unimolecular dissociation as the dominant means by which energy can be dissipated. The calculated average temperatures of the clusters in this study range from 260 to 890 K (Table 2). They provide a convenient measure for the internal energy content of the ion clusters and are essential for analyzing structural aspects of these ion clusters by Monte Carlo techniques.

**B. Monte Carlo Simulations.** MC simulations using the polarizable potential have been performed on $Na^+(CH_3OH)_{1-8}$.

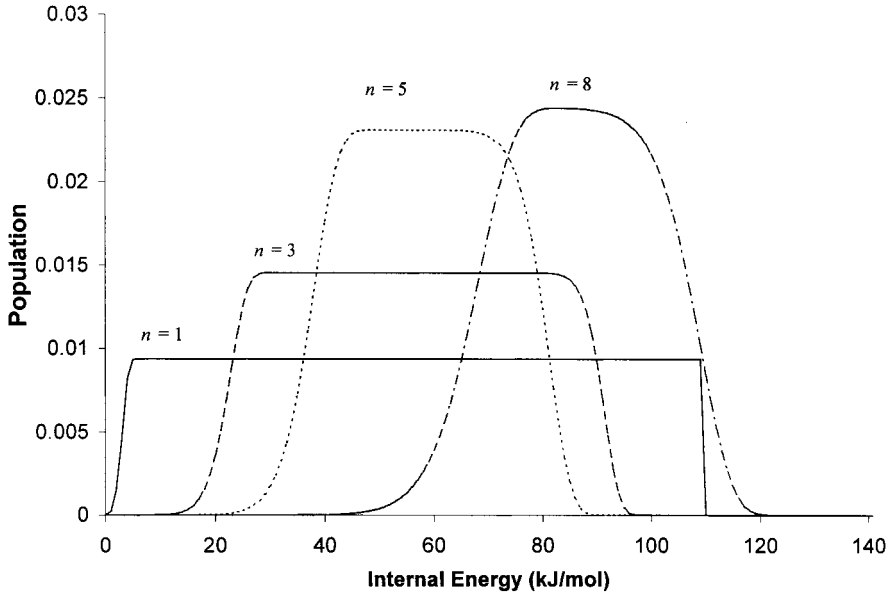


**Figure 5.** Calculated internal energy distributions of $Na^+(CH_3OH)_n$. The binding energies are distinctly narrower when five or more solvent molecules are present. The widths of the distributions follow binding energy trends.

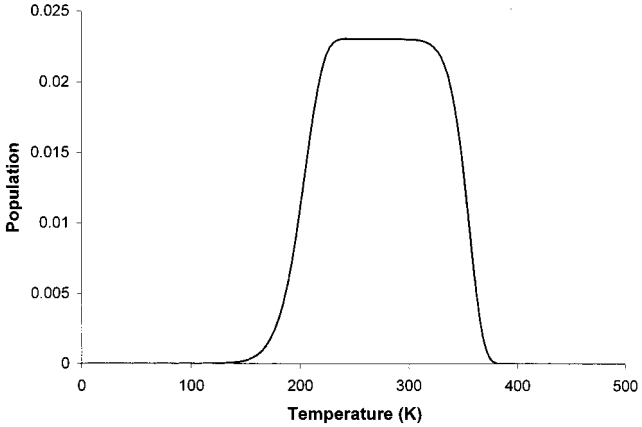


**Figure 6.** Calculated temperature distribution of $Na^+(CH_3OH)_5$. This reflects the broad internal energy distribution and nonthermal behavior of the cluster ions.

Temperatures were chosen to correspond with cluster internal energies/temperatures in our molecular beam experiments as discussed above and summarized in Table 2. The MC simulation for $Na^+(CH_3OH)_1$ was performed at a significantly lower temperature than suggested by the RRKM/EE calculations since, at higher temperatures, the solvent molecule would experience "walk-off", the MC equivalent of evaporative loss.

The calculated RDFs of the methanol atoms with respect to the $Na^+$ ion are displayed in Figure 7a for $Na^+(CH_3OH)_1$. The Figure shows that the oxygen atom, with a maximum at 2.2 Å, is in closest proximity to the ion as would be expected based on the molecule's dipole moment and associated charge distribution. The carbon atom and hydroxyl hydrogen atom are further away at 2.9 and 3.0 Å, respectively, indicating that the methyl group is canted over toward the ion. The ion−atom RDFs for the cluster ion $n = 8$, presented in Figure 7b, show two distinct peaks for each atom, indicating the presence of a first and second shell. Focusing on the first shell features, we observe that the oxygen peak shifts slightly outward to 2.3 Å, reflecting the overall weaker interaction between the ion and each individual molecule in the presence of multiple solvents. Curiously, the hydroxyl hydrogen atom peak is constant at 3.0 Å for each cluster size. The carbon atom peak, however, slowly

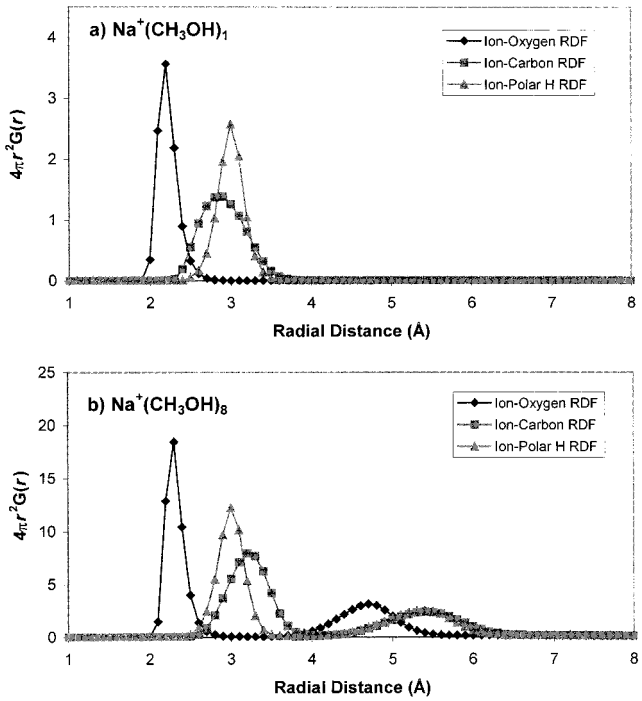


**Figure 7.** Ion−atom site radial distribution functions for (a) $Na^+(CH_3OH)_1$ and (b) $Na^+(CH_3OH)_8$. The second set of peaks observed in (b) is due to the formation of a second solvent shell. Note that while the first solvent shell ion−oxygen and ion−hydrogen RDF peaks are unchanged between $n = 1$ and $n = 8$, the ion−carbon RDF peak has a significant shift.

shifts to larger distance with increasing cluster size, ending at 3.2 Å for $Na^+(CH_3OH)_8$. This is probably due to steric repulsion between the solvents in the first solvation shell. As more solvents are added and take positions next to the ion, there is less room for the sterically bulky methyl groups. The methanol thus rotates slightly, shifting the methyl group further away from the ion.

In Figure 8a, we concentrate on the $Na^+$−O RDFs for $Na^+(CH_3OH)_{1-8}$. The narrow peak centered at 2.2 Å corresponds to the methanol molecules in the first solvation shell about the ion. The limited width (0.2 Å full width at half-maximum) of the peak attests to the strong influence of the ion

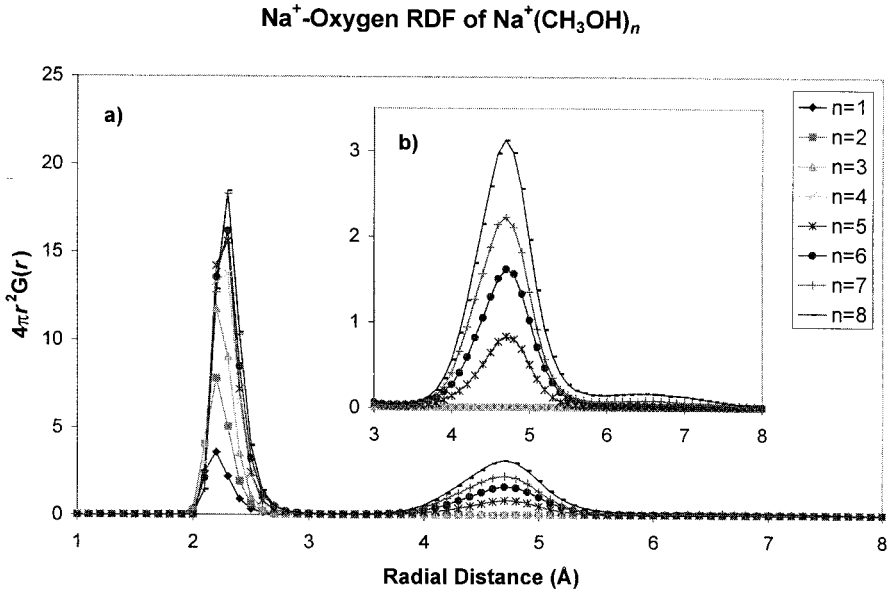


**Figure 8.** Ion−oxygen radial distribution functions. (a) The peak centered about 2.4 Å is due to methanols in the first solvation shell. The second peak, seen more clearly in (b), corresponds to occupation in the second solvent shell.

**TABLE 5: Calculated Occupancy of the Different Solvation Shells about the Ion Determined by Integrating over the Peaks in the $Na^+$−O RDFs**

| $Na^+(CH_3OH)_n$ | first shell | occupancy second shell | third shell |
|---|---|---|---|
| 1 | 1.00 | | |
| 2 | 2.00 | | |
| 3 | 3.00 | | |
| 4 | 3.98 | 0.02 | |
| 5 | 4.31 | 0.68 | 0.01 |
| 6 | 4.57 | 1.39 | 0.04 |
| 7 | 4.91 | 1.94 | 0.15 |
| 8 | 4.97 | 2.75 | 0.28 |

on the solvent molecules in the first shell. The second peak at 4.7 Å is due to solvents in the second solvation shell and is considerably broader at 0.8 Å (fwhm). This is a direct consequence of the much weaker electrostatic interaction that binds the second shell solvents to the cluster. For $n = 7$, a feature centered at about 6.5 Å with a fwhm of 1.6 Å suggests occupation in a third solvent shell which becomes more distinct at $n = 8$. The ion−solvent radial distribution functions underscore the effect of the ion on the local solvent structure. Solvents adjacent to the ion are rigidly structured, whereas those positioned further away from the ion have a more fluid nature, as directly evidenced by the increased broadness of the solvent shell peaks in the RDFs with increasing ion−solvent distance.

The occupancy numbers for each solvent shell are determined by integrating the RDFs and are listed in Table 5. The noninteger character of some of the results is due to isomerization between different cluster ion configurations. The integration limits were selected by determining the minima between the solvent shell peaks in the RDFs. The first shell cutoff was set at 3.4 Å, and the second shell cutoff at 5.7 Å. The table shows that the occupancy of the first shell rises with increasing cluster ion size, culminating in a first solvent shell size of ∼5 at $n = 8$. The first significant occupation of a second solvation shell is observed for $n = 5$ (probability = 0.68). Not surprisingly, second shell occupancy continues to increase for the larger clusters. Discernible occupation of a third solvation shell does not appear until $n = 7$, as shown in Figure 8b.

*1. Structural Configurations of $Na^+(CH_3OH)_{1-4}$.* The smallest cluster ions, $Na^+(CH_3OH)_{1-4}$, have all the methanols residing in the first solvation shell. Representative MC structural

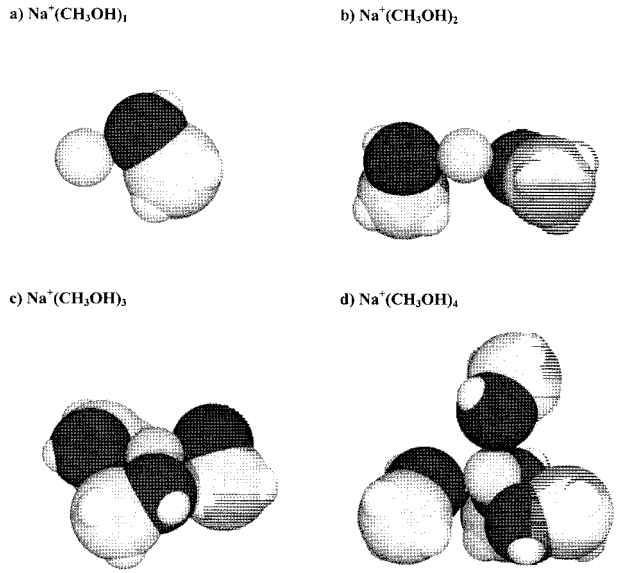


**Figure 9.** Structural configurations of $Na^+(CH_3OH)_{1-4}$. (b) In the case of $n = 2$, the solvents have a slight tendency to congregate onto one side of the ion. The cluster ion adopts a symmetric trigonal planar structure for (c) $n = 3$ and a tetrahedral structure for (d) $n = 4$.

snapshots of each are presented in Figure 9. Averaging the angle, $\angle O_1-Na^+-O_2$, over all methanol pairs yields the distribution displayed in Figure 10 for $Na^+(CH_3OH)_{2-4}$. Surprisingly, the distribution does not peak at 180° for $n = 2$, but at 128°, indicating that the two methanols show a preference to one side. This is probably due to a slight polarization of the $Na^+$ by the first molecule, which biases the positioning of the second molecule. The calculated averages from the angular distributions are 130 ± 21°, 116 ± 18°, and 109 ± 17° for the $n = 2$, 3, and 4 cluster ions, respectively, the latter two being close to the expected values of 120° and 109.5° for trigonal and tetrahedral structures.

*2. Structural Configurations of $Na^+(CH_3OH)_5$.* The initial presence of methanol in the second solvent shell for $n = 5$ (see Table 5) is suggestive of hydrogen bond formation between the second shell methanol molecule with a counterpart in the first shell. To determine whether a hydrogen bond has actually

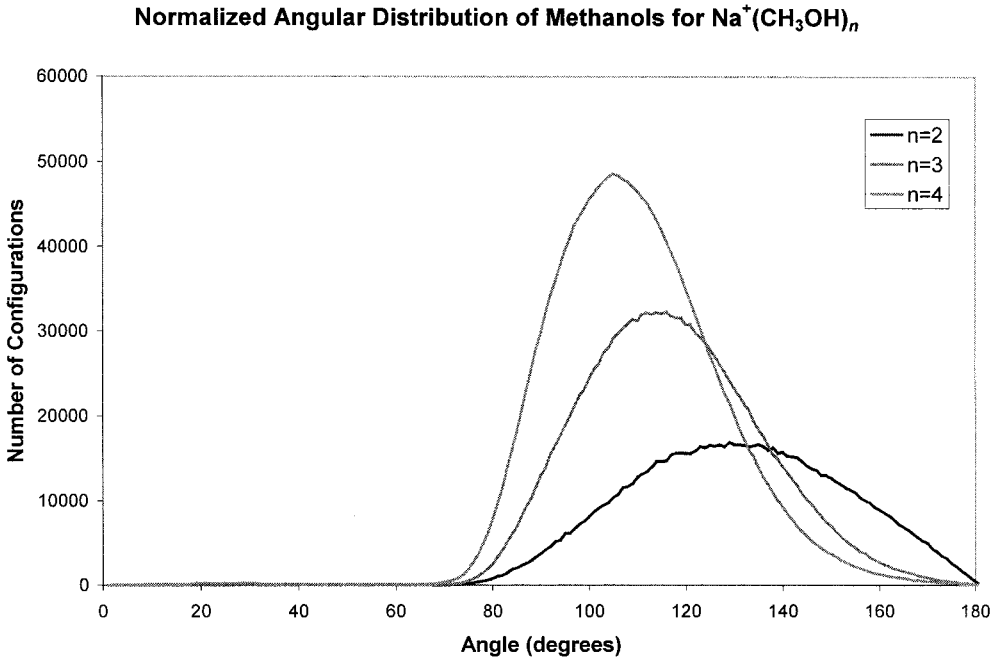


**Figure 10.** Methanol−methanol angular distribution plot for $Na^+(CH_3OH)_{2-4}$.

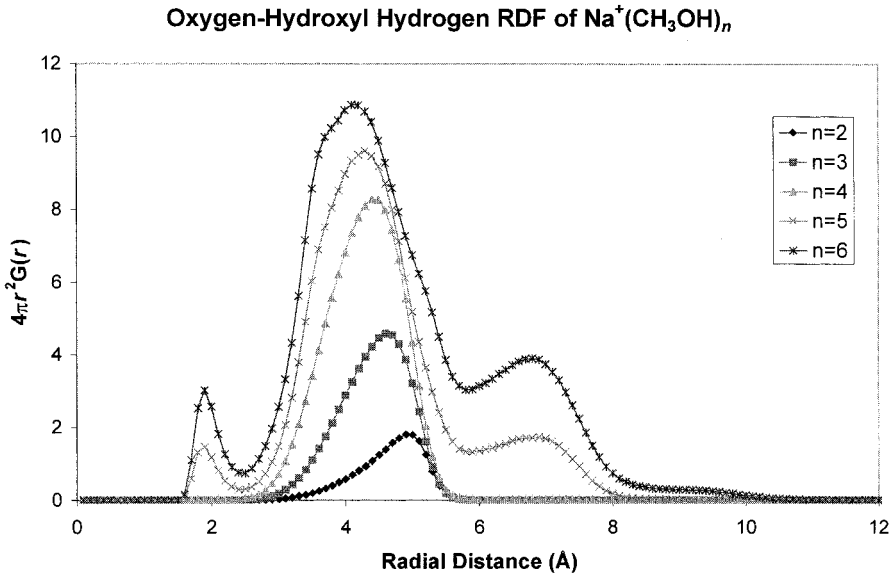


**Figure 11.** The oxygen−hydroxyl hydrogen radial distribution function. Multiple peaks are not observed until $n \geq 5$, which also coincides with the first observation of second shell structure and hydrogen bonding.

formed, we turn to the methanol−methanol RDFs of $Na^+(CH_3OH)_{2-6}$ plotted in Figure 11. These represent the radial distribution of the hydroxyl hydrogen atoms to the oxygen atom site on different methanol molecules. A dominant peak in the 4.1−4.9 Å range is observed for all cluster sizes and is attributed to the average distance between the methanol molecules in the first solvation shell. This peak slowly shifts to smaller distance with larger cluster size as the number of methanol in the first shell increases, reflecting the crowding of the solvent shell. Two additional peaks first appear for $Na^+(CH_3OH)_5$. The small peak at 1.9 Å is attributed to the formation of a hydrogen bond. The presence of the second peak at 6.8 Å is due to the greater distance between the hydroxyl atoms of the first shell methanol molecules and the oxygen atom of the second shell methanol. The absence of these two peaks in the distributions of $Na^+(CH_3OH)_{2-4}$ indicates that there is no hydrogen bond formation in the smallest cluster ions. Integration of the hydrogen bond peak yields the average number of hydrogen bonds to be 0.67, consistent with the occupancy number of the second solvent shell for $n = 5$. This technique presumes that all hydrogens within a certain distance of an oxygen atom result in the formation of a hydrogen bond. A more rigorous definition of hydrogen bond formation additionally requires a hydrogen bond angle of 145° and 180° for the angle formed by the donor oxygen, donor hydrogen, and acceptor oxygen atoms.[29] The results of this analysis are presented in Table 6, along with the average hydrogen bond length and angle, which remain relatively constant regardless of cluster ion size.

The two main structural isomers observed for $Na^+(CH_3OH)_5$ are displayed in parts a and b of Figure 12. One contains all five solvent molecules in the first solvation shell in a "5 + 0" configuration specifying the number of solvents in the first and second solvent shell, respectively. The second structure has a "4 + 1" configuration where the second shell methanol is predominantly hydrogen bonded to a single first shell methanol. At certain points, however, it does act as a double acceptor to

**TABLE 6: Average Hydrogen Bond Properties**

| $Na^+(CH_3OH)_n$ | no. of H-bonds | hydrogen bonds O···H distance (Å) | ∠O−H···O |
|---|---|---|---|
| 3 | 0.00 | | |
| 4 | 0.01 | 1.98 | 160.9° |
| 5 | 0.57 | 1.93 | 162.1° |
| 6 | 1.20 | 1.95 | 161.9° |
| 7 | 1.87 | 1.96 | 162.1° |
| 8 | 2.69 | 1.96 | 162.1° |

two first shell solvents as shown in Figure 12c. The double acceptor configuration serves as an intermediate between the transfer of the hydrogen-bonded methanol from one first shell molecule to another. It is interesting to note that the point at which hydrogen bonds can first exist is also matched by the occurrence of structural isomers.

To better quantify the probabilities of each of the different structural configurations, the $Na^+$−methanol oxygen distances were examined every 500 MC steps. The solvent shell cutoffs given by the $Na^+$−O RDFs were used to determine whether the cluster was in a "5 + 0" or "4 + 1" configuration. The resulting isomer distribution reveals that the "4 + 1" configuration has an existence probability of 0.68. This corroborates the results of the $Na^+$−O RDF integration which indicate that there is a probability of 0.68 of a methanol in the second solvent shell. Although, the determination of the isomer distribution in the case of $n = 5$ appears trivial, it will prove more useful in the examination of the larger cluster ions.

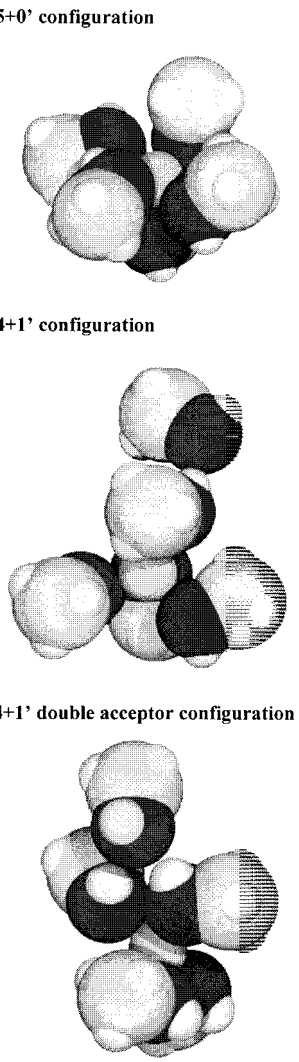


**Figure 12.** Structural configurations of $Na^+(CH_3OH)_5$. The two major groups of isomers have either (a) five or as in (b) and (c) four solvents in the first solvation shell. The second shell methanol can be secured to the ion by either one or two hydrogen bonds to methanols in the first solvent shell as shown in (b) and (c), respectively.

**TABLE 7: Distribution of Structural Isomers for $Na^+(CH_3OH)_{4-8}$**

| $Na^+(CH_3OH)_n$ | first shell | occupancy second shell | third shell | contribution[a] (%) |
|---|---|---|---|---|
| 4 | 4 | | | 98.4 |
| 5 | 5 | | | 31.2 |
| | 4 | 1 | | 67.9 |
| 6 | 5 | 1 | | 52.9 |
| | 4 | 2 | | 41.5 |
| 7 | 5 | 2 | | 71.2 |
| | 5 | 1 | 1 | 9.6 |
| | 4 | 3 | | 7.9 |
| | 4 | 2 | 1 | 6.1 |
| | 6 | 1 | | 5.1 |
| 8 | 5 | 3 | | 60.6 |
| | 5 | 2 | 1 | 20.8 |
| | 6 | 2 | | 7.1 |
| | 4 | 3 | 1 | 5.8 |

[a] Evaluated at simulation temperatures given in Table 4. Only contributions greater than 5% are listed.

*3. Structural Configurations of $Na^+(CH_3OH)_{6-8}$.* The solvation shell occupancy numbers and configurations for $Na^+(CH_3OH)_6$ are contained in Tables 5 and 7. The data indicate that the cluster is primarily in a "5 + 1" configuration with a probability of 0.53 and a substantial contribution from a "4 + 2" configuration leading to the formation of 1.20 hydrogen bonds. Figure 13 displays snapshots of the MC simulation corresponding to these possible configurations. Double acceptor configurations are observed for both the "5 + 1" and the "4 + 2" configurations as seen in part c and d of Figure 13. Minor contributions from two additional structural isomers, consisting of "6 + 0" and "4 + 1 + 1" configurations, were also observed. The presence of the latter configuration, displayed in Figure 13e, is due to the formation of a hydrogen-bonded chain. Although the MC simulations are conducted at a single temperature for each cluster, the experiments probe cluster ions with a distribution of temperatures. Thus, the "4 + 1 + 1" structure for $Na^+(CH_3OH)_6$ only accounts for 3% of the observed isomers at a simulation temperature of 275 K, while 7% of the cluster ions appear to be in a "4 + 1 + 1" configuration at 300 K.

Not unexpectedly, the amount of hydrogen bonding continues to increase with the addition of a seventh methanol molecule. There are now, on average, 1.87 hydrogen bonds per cluster ion. The vast majority of the cluster ions form a structure that contains five first shell methanol molecules and two methanols in the second shell. Four other structural isomers are present with contributions between 5% and 10%, as given in Table 7.

A myriad of structural isomers are found in the MC simulations of $Na^+(CH_3OH)_8$, as the larger number of solvent molecules continues to augment the number of possible configurations. On average, there are 2.69 hydrogen bonds formed. Again there was a dominant configuration consisting of the "5 + 3" isomer at 61%, while the "5 + 2 + 1" configuration was a significant minority accounting for another 21%. Two minor contributions were found: a "6 + 2" and a "4 + 3 + 1" configuration. It appears that as the number of methanol solvents increases, so does the occupancy of the first solvation shell. This is in accord with studies of $Na^+$ solvation in bulk liquid, which indicate a first solvent shell size of six methanols.[54] All of the different isomer distributions for each of the larger cluster sizes are listed in Table 7.

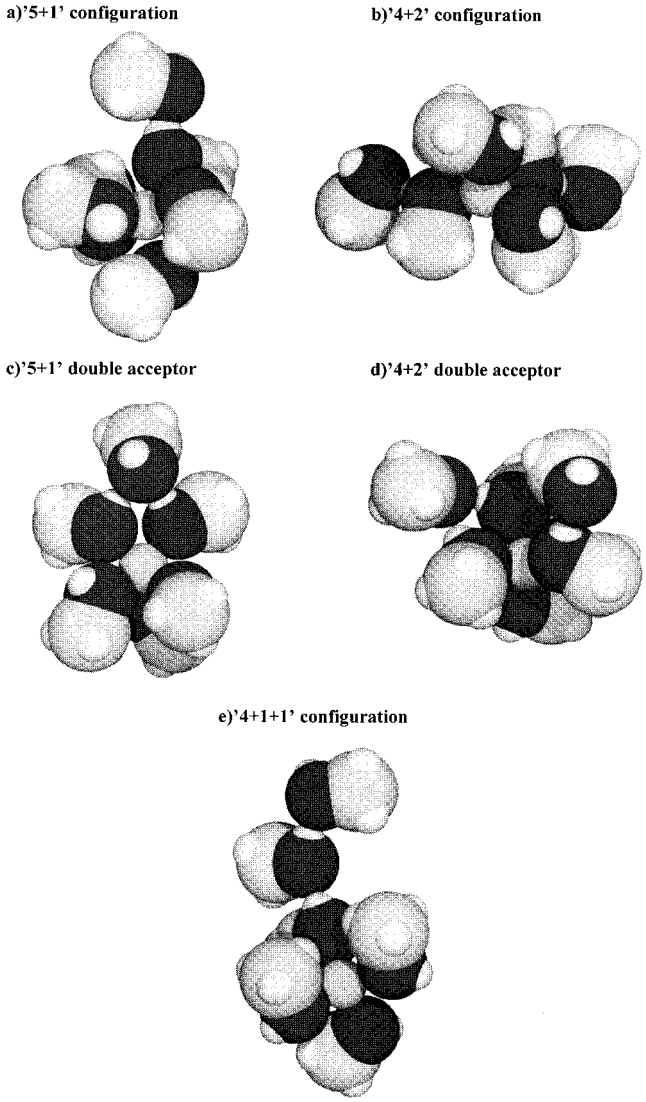


**Figure 13.** Structural configurations of $Na^+(CH_3OH)_6$. Two major isomer groupings have either (a) five or (b) four solvent molecules in the first solvent shell. Double acceptor configurations are also observed for both the (c) "5 + 1" and (d) "4 + 2" cluster ion configurations. As displayed in part e, the $n = 6$ cluster ion can also adopt a configuration where three methanols molecules line up to form a hydrogen bonded chain.

The polarizable potential used in this study has clearly led to a distinct difference from previous MC studies[29,51,54] in that hydrogen bond formation occurs before the filling of the first solvent shell.

*4. Cluster Ion Energy Distributions.* Table 8 summarizes the total energy of each cluster along with the contributions from the ion−solvent interaction, the solvent−solvent interaction, and the polarization energy. In the small clusters, $n = 2-4$, the solvent−solvent interaction energy slowly increases due to steric repulsion. As more molecules are added to the first solvation shell, they are forced closer together (recall the angular distribution plot, Figure 10), resulting in a larger repulsive interaction. Also, the relative contribution of the polarization to the total potential energy steadily decreases from 33% for $n = 1$ to 19% for $n = 4$, an example of a microscopic dielectric effect. Overall, it is not surprising that the magnitude of the total potential energy steadily increases with the addition of each solvent molecule. While partly an effect due to the lower temperatures of the larger simulations (see Figure 2 and Table 2), it is mainly attributed to the additional binding energy of the extra methanol.

**TABLE 8: Average Total Energy of the Cluster Ion and the Average Contributions Due to Each of the Different Cluster Interactions for $Na^+(CH_3OH)_{1-8}$[a]**

| $Na^+(CH_3OH)_n$ | ion−solvent (kJ/mol) | solvent−solvent (kJ/mol) | polarization (kJ/mol) | total energy (kJ/mol) |
|---|---|---|---|---|
| 1 | −67 (8) | 0 | −31 (7) | −98 (7) |
| 2 | −138 (9) | 2 (1) | −52 (7) | −187 (8) |
| 3 | −211 (10) | 7 (3) | −62 (6) | −266 (8) |
| 4 | −283 (12) | 16 (5) | −64 (5) | −331 (10) |
| 5 | −321 (23) | 14 (13) | −67 (8) | −374 (9) |
| 6 | −350 (26) | 10 (14) | −69 (8) | −410 (11) |
| 7 | −385 (24) | 7 (13) | −70 (7) | −448 (11) |
| 8 | −405 (23) | −2 (13) | −73 (7) | −480 (12) |

[a]The values in parentheses represent one standard deviation.

For the larger cluster ions, $Na^+(CH_3OH)_{5-8}$, there are a number of notable trends. First, there is only gradual growth in the polarization energy. Second, the solvent−solvent interaction changes from repulsive to attractive and at a sharper rate of growth than the polarization energy. This is to be expected. Attractive solvent−solvent interactions should dominate as the second and third solvent shells fill. Conversely the ion−solvent interaction should plateau as the inner solvent shells shield the ion, a trend which is also observed.

It is interesting to see how the different isomers contribute to the energy of the cluster. We examine $Na^+(CH_3OH)_5$, since that is the first cluster ion for which a significant number of isomers are observed in the simulation. Figure 14 displays the total energy and its three components for the cluster over the course of the simulation. Although the individual contributions have bimodal distributions, the total energy remains evenly distributed about −380 kJ/mol. (Of course, if this were not true, one isomer would be lower in energy than the others and result in the presence of a single configuration.) The bimodality of the different individual energy contributions is attributable to the two structural isomers found for $Na^+(CH_3OH)_5$. It is simple to assign which structures are responsible for the two different peaks of each energy distribution by first considering the ion−solvent energy. This energy will be lowest when all five solvents are arranged around the ion. Thus, the peak at −355 kJ/mol is due to the "5 + 0" configuration. Since this configuration will lead to a large steric interaction, the corresponding solvent−solvent energy peak must be at +30 kJ/mol. To yield a total energy of −380 kJ/mol, the appropriate polarization energy peak is at −55 kJ/mol.

The unassigned peaks thus belong to the "4 + 1" cluster configuration making the ion−solvent, the solvent−solvent, and the polarization energy contributions −310, +5, and −70 kJ/mol, respectively. The less favorable ion−solvent interaction energy for the "4 + 1" is partially offset by a decrease in the steric repulsion between the first shell solvents and a more favorable neutral−neutral interaction due to the formation of the hydrogen bond. A lowering of the polarization potential energy compensates for the remaining difference. The larger contribution to the total energy by the polarization energy term upon hydrogen bond formation supports the contention that cooperativity effects enhance the strength of the hydrogen bond. Similar trends are observed in the larger cluster ions.

These data underscore the subtle interplay between the various intermolecular forces present in the cluster. While the formation of a hydrogen bond between a first and second shell solvent molecule is favorable, it comes at the loss of a potentially stronger ion−solvent interaction. The difference is offset by a

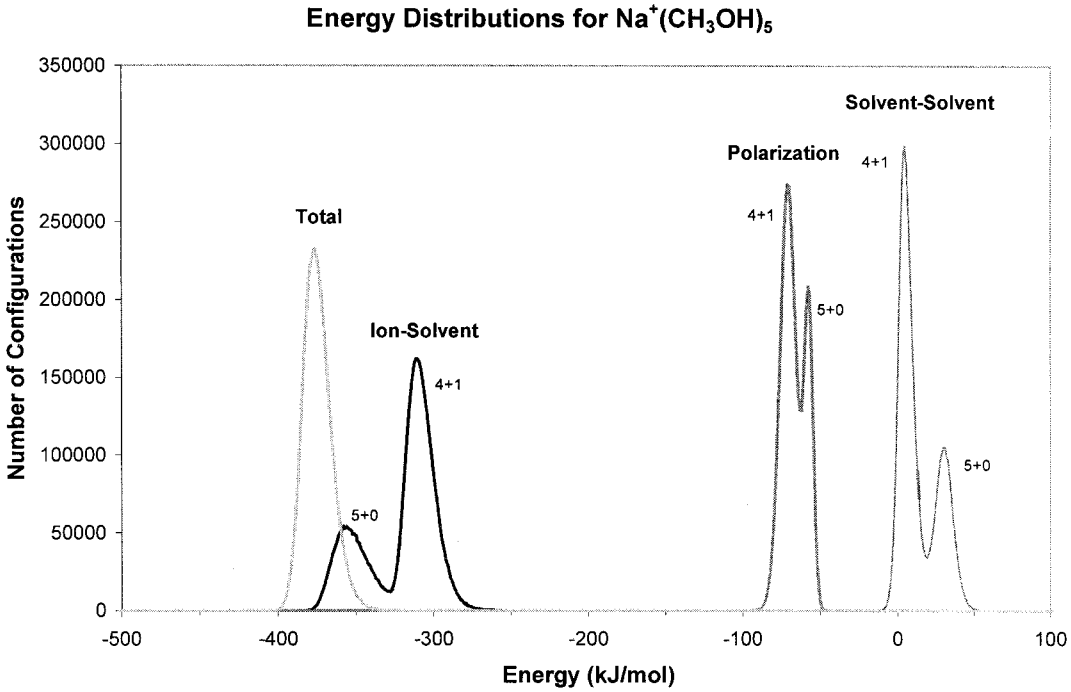


**Figure 14.** Ion−solvent, solvent−solvent, polarization, and total energy distribution for $Na^+(CH_3OH)_5$. The two major isomeric forms yield different contributions to the ion−solvent, solvent−solvent, and polarization energies of the cluster ion yet sum up to the same total energy.

decrease in the sterically repulsive interaction energy between first shell solvents. The cluster ion structure is ultimately determined by the competition between the different intermolecular forces present. The polarizable potential is able to accurately model these subtleties and yield experimentally consistent cluster ion structures as will be seen below.

**C. Vibrational Predissociation Spectroscopy of $Na^+(MeOH)_n$.** The motivation for performing the MC simulations is to provide insight into the experimentally determined vibrational dissociation spectra of the cluster ions. A detailed analysis of the vibrational spectroscopy of $Na^+(CH_3OH)_{2-7}$ in the 3200−3800 $cm^{-1}$ region is provided elsewhere,[30,47] so a brief synopsis is presented here to better contrast the MC simulation data. The spectra of $Na^+(CH_3OH)_{2-4}$ are dominated by a single band in the 3660−70 $cm^{-1}$ region, which grows in intensity with the number of methanols. The position of the band is only slightly shifted from the gas-phase value of 3681 $cm^{-1}$ for the O−H stretch in methanol, which indicates that the solvent is oriented with the O−H group pointing away from the ion and other methanols. There is a small feature near 3400 $cm^{-1}$ about 1/10 of the intensity of the 3670 $cm^{-1}$ band for $Na^+(CH_3OH)_4$, suggesting that a small amount of a hydrogen-bonded structural isomer is present starting at that size (see Figures 1 and 3 in ref 30).

The spectra of $Na^+(CH_3OH)_{5-7}$ are dominated by absorption bands in the region from 3300 to 3600 $cm^{-1}$, indicating extensive hydrogen bonding of the methanol O−H groups. Bands near 3420 and 3510 $cm^{-1}$ are observed for all three cluster ions, while an additional band near 3350 $cm^{-1}$ was found for $Na^+(CH_3OH)_{6,7}$. The spectra of $Na^+(CH_3OH)_{5-7}$ also contained as a minor feature the band at 3670 $cm^{-1}$ (see Figure 2 in ref 30). The O−H bands in the hydrogen-bonded region were previously interpreted to be due to small methanol aggregates: dimers, trimers, and tetramers that were then complexed to the ion.[30] However, in light of the MC results given above as well as recent spectroscopic results of the $K^+(C_6H_6)_n(H_2O)_m$ (refs14 and 15) cluster ion system and nitrogen matrix studies of methanol clusters,[59] a new interpretation of the hydrogen-bonded features of the vibrational spectra of $Na^+(CH_3OH)_n$ will be presented below.

In the IR spectrum of $Na^+(CH_3OH)_n$, extensive evidence for hydrogen bonding is first observed for $n = 5$, an observation that is consistent with the Monte Carlo simulations presented above. Considering that the main structural isomer observed for $n = 5$ consists of the cluster in a "4 + 1" configuration, the infrared band near 3420 $cm^{-1}$ is attributed to the formation of a hydrogen bond. It is assigned to the O−H group in the first shell methanol which forms a hydrogen bond with a methanol in the second shell. In neutral methanol dimer, the hydrogen-bonded O−H stretch is observed[60] at 3574 $cm^{-1}$, shifted ∼100 $cm^{-1}$ to lower frequency from the monomer. The presence of the ion serves to cooperatively polarize the hydrogen bond and shift the first shell methanol O−H stretch an additional 150 $cm^{-1}$ to lower frequency. A similar comparison can be made in the hydrogen-bonded O−H stretch of water in $K^+(C_6H_6)_3(H_2O)_2$, where a water molecule in the first shell is hydrogen bonded to a water in the second shell.[14,15] In analogy to methanol, the hydrogen-bonded O−H stretch of neutral water dimer[61] is observed at 3600 $cm^{-1}$, shifted ∼100 $cm^{-1}$ from the O−H stretch of water monomer.[62] The presence of the potassium ion shifts the O−H stretch an additional 110 $cm^{-1}$ to lower frequency, 3486 $cm^{-1}$, in the $K^+(C_6H_6)_3(H_2O)_2$ system. Clearly the presence of the ion cooperatively enhances the strength of the hydrogen bond, lowering the O−H stretching frequency in both $K^+(C_6H_6)_3(H_2O)_2$ and $Na^+(CH_3OH)_5$.

The remaining peak near 3510 $cm^{-1}$ in the spectrum of $Na^+(CH_3OH)_5$ must be due to a different and weaker hydrogen-bonded feature. This may occur when two first shell methanols simultaneously hydrogen-bond to a single second shell methanol. The first shell methanols form 'bent' hydrogen bonds, i.e., the O−H···O angles deviate from the optimal 180° linear configuration thus weakening this highly directional interaction. Such types of "bent" hydrogen bonds have been postulated by Robinson[63] to explain anomalies in the condensed phases of water. Furthermore, hydrated alkali metal ion structures with two first shell waters donating to the same second shell water

molecule have been found as minima in ab initio structure calculations.[64] For $Na^+(H_2O)_5$, this double acceptor structure is ~2.5 kcal/mol less stable than the globally minimized single acceptor "4 + 1" configuration.[64] The similarity between water and methanol suggests that similar types of bonding should be possible in $Na^+(CH_3OH)_5$. Recall, that the MC simulations also show evidence of a double acceptor structure beginning with the $Na^+(CH_3OH)_5$, further corroborating the vibrational assignment of the band at 3510 $cm^{-1}$ to a double acceptor configuration.

The infrared spectrum of $Na^+(CH_3OH)_6$ introduces a new feature near 3350 $cm^{-1}$ in addition to the bands observed in the smaller $n = 5$ cluster. This is assigned to a cooperatively enhanced hydrogen bond resulting from the formation of a hydrogen bond chain; an outer shell methanol molecule hydrogen bonds to a molecule in the second shell which is hydrogen bonded to a first shell methanol. The methanol in the first shell will be strongly polarized by the ion and the two outer molecules resulting in an enhanced hydrogen bond. A similar observation was made for the hydrogen bonded chain in neutral methanol trimer, where the O−H stretch of the middle methanol molecule is cooperatively enhanced by interaction with the two adjacent methanol molecules.[59,65] Indeed the middle methanol O−H frequency of 3390 $cm^{-1}$ is conspicuously close to the band observed near 3350 $cm^{-1}$ in $Na^+(CH_3OH)_6$. This interpretation also suggests that the cooperativity effects associated with the formation of longer hydrogen bond chains would enhance the strength of the hydrogen bonds and shift the corresponding O−H stretching modes to even lower vibrational frequencies. These extended chain structures have been observed in the MC simulations of $Na^+(CH_3OH)_6$, again directly supporting the vibrational assignment. The remaining peaks are assigned similarly to those observed in the spectrum of $Na^+(CH_3OH)_5$.

The addition of a seventh methanol molecule further increases the intensity of the hydrogen bond features in the spectrum. This is indicative of the progressive formation of hydrogen bonds. The continued addition of solvent molecules will eventually lead to a broad absorption with no easily resolvable features resulting in the need for a finer structural probe. The MC simulations of $Na^+(CH_3OH)_{7,8}$ support this interpretation. The simulations show that the larger cluster ions continue to form more hydrogen bonds and several different isomers. Both of these increasing trends serve to complicate and broaden the vibrational spectra of the cluster ions.

In summary, the infrared spectral features of the O−H stretching modes in $Na^+(CH_3OH)_{2-7}$ are readily interpreted by structures that arise from the Monte Carlo simulations. The polarizable potential used in the simulations is able to reflect the competition between the various noncovalent interactions. Furthermore, the results from the simulations are in qualitative agreement with the experimental observations, in that the cluster size corresponding to the onset of extensive hydrogen-bonded structures is consistent with experiment, as is the existence of structural isomers.

## VI. Conclusions

The detailed analysis of gas-phase cluster ions has been hampered by an inability to assess the amount of internal energy contained within these species. We have presented here an experimental approach, which is sensitive to the presence of significant amounts of internal energy through the detection of solvent evaporation. This allows evaluation of an average unimolecular dissociation rate for the loss of one solvent. These experimental rates can then be compared with calculated values based on computed internal energy distributions derived from RRKM theory and the evaporative ensemble for isolated clusters. The agreement between the calculated and experimental rates gives support to the accuracy of the determined internal energy distributions for the cluster ions generated in the apparatus. The analysis requires accurate binding energies and vibrational frequencies, essential information supplied in part by the efforts of other research groups.

Significant amounts of internal energy can complicate the analysis of other experimental attributes of cluster ions, such as the infrared spectra. Monte Carlo simulations using a polarizable potential model were performed on $Na^+(CH_3OH)_{1-8}$ to examine the structural properties at temperatures consistent with the energized cluster ions in our apparatus. Structural features that are dependent on both size and temperature, such as the onset of hydrogen bonding and the types of hydrogen bonded structures, could then be compared with characteristic O−H stretching frequencies from infrared spectra. The first size, at which considerable hydrogen bonding was observed experimentally, was five solvents, a result consistent with predictions from the MC simulations. The existence of multiple structural isomers with the onset of hydrogen bond formation was also consistent between simulation and experiment. The types of hydrogen bonded structures: single and double first shell donors, and linear chain species, predicted from the simulations led to a revised assignment of O−H hydrogen-bonded features, underscoring the important synergism between experimental and theoretical methods for these larger cluster ion species.

The methods presented here permit the determination of cluster ion internal energy distributions and assessment of its impact on a variety of experimental properties. The method can also be applied to other experimental techniques where spontaneously evaporating cluster ions are generated, and should prove useful in characterizing the internal energy distributions of cluster ions generated by other groups.

**Acknowledgment.** This research is supported in part by the National Science Foundation through Grant CHE-9700722. We thank Prof. Todd Martínez for determining the vibrational frequencies of $Na^+(CH_3OH)_{1-4}$ and Prof. Zaida Luthey-Schulten for helpful comments on the manuscript.

## References and Notes

(1) Castleman, A. W., Jr.; Bowen, K. H., Jr. *J. Phys. Chem.* **1996**, *100*, 12911.
(2) Lisy, J. M. *Int. Rev. Phys. Chem.* **1997**, *16*, 267.
(3) Duncan, M. A. *Annu. Rev. Phys. Chem.* **1997**, *48*, 69.
(4) Syage, J. A. *J. Phys. Chem.* **1995**, *99*, 5772.
(5) Dunbar, R. C. *J. Phys. Chem.* **1994**, *98*, 8705.
(6) Dunbar, R. C.; McMahon, T. B.; Tholmann, D.; Tonner, D. S.; Salahub, D. R.; Wei, D. Q. *J. Am. Chem. Soc.* **1995**, *117*, 12819.
(7) Dunbar, R. C.; McMahon, T. B. *Science* **1998**, *279*, 194.
(8) Ferhati, A.; McMahon, T. B.; Ohanessian, G. *J. Am. Chem. Soc.* **1996**, *118*, 5997.
(9) Schindler, T.; Berg, C.; Niednerschatteburg, G.; Bondybey, V. E.; Lugez, C.; Schriver, A.; Schriver, L. *J. Phys. Chem.* **1994**, *98*, 4316.
(10) Schindler, T.; Berg, C.; Niednerschatteburg, G.; Bondybey, V. E. *Chem. Phys. Lett.* **1996**, *250*, 301.
(11) Weinheimer, C. J.; Lisy, J. M. *Chem. Phys.* **1998**, *239*, 357.
(12) Cabarcos, O. M.; Lisy, J. M. *Int. J. Mass Spectrom.* **1998**, *185−187*, 883.
(13) Cabarcos, O. M.; Lisy, J. M. *Chem. Phys. Lett.* **1996**, *257*, 265.
(14) Cabarcos, O. M.; Weinheimer, C. J.; Lisy, J. M. *J. Chem. Phys.* **1998**, *108*, 5151.
(15) Cabarcos, O. M.; Weinheimer, C. J.; Lisy, J. M. *J. Chem. Phys.* **1999**, *110*, 8429.
(16) Choi, J.-H.; Kuwata, K. T.; Cao, Y.-B.; Okumura, M. *J. Phys. Chem.* **1998**, *102*, 503.

(17) Ayotte, P.; Bailey, C. G.; Weddle, G. H.; Johnson, M. A. *J. Phys. Chem. A* **1998**, *102*, 3067.
(18) Ayotte, P.; Weddle, G. H.; Kim, J.; Johnson, M. A. *Chem. Phys.* **1998**, *239*, 485.
(19) Ayotte, P.; Weddle, G. H.; Kim, J.; Johnson, M. A. *J. Am. Chem. Soc.* **1998**, *120*, 12361.
(20) Dorsett, H. E.; Watts, R. O.; Xantheas, S. S. *J. Phys. Chem. A* **1999**, *103*, 3351.
(21) Nizkorodov, S. A.; Dopfer, O.; Ruchti, T.; Meuwly, M.; Maier, J. P.; Bieske, E. J. *J. Phys. Chem.* **1995**, *99*, 17118.
(22) Nizkorodov, S. A.; Meuwly, M.; Maier, J. P.; Dopfer, O.; Bieske, E. J. *J. Chem. Phys.* **1998**, *108*, 8964.
(23) Dopfer, O.; Olkhov, R. V.; J. P.; M. *J. Phys. Chem.* **1999**, *103*, 2982.
(24) Olkhov, R. V.; Nizkorodov, S. A.; Dopfer, O. *J. Chem. Phys.* **1998**, *108*, 10046.
(25) Dopfer, O.; Nizkorodov, S. A.; Meuwly, M.; Bieske, E. J.; Maier, J. P. *Int. J. Mass Spectrom. Ion Processes* **1997**, *167/168*, 637.
(26) France, M. R.; Pullins, S. H.; Duncan, M. A. *J. Chem. Phys.* **1998**, *109*, 8842.
(27) France, M. R.; Pullins, S. H.; Duncan, M. A. *Chem. Phys.* **1998**, *239*, 447.
(28) Pullins, S. H.; Reddic, J. E.; France, M. R.; Duncan, M. A. *J. Chem. Phys.* **1998**, *108*, 2725.
(29) Selegue, T. J.; Moe, N.; Draves, J. A.; Lisy, J. M. *J. Chem. Phys.* **1992**, *96*, 7268.
(30) Weinheimer, C. J.; Lisy, J. M. *J. Phys. Chem.* **1996**, *100*, 15305.
(31) Klots, C. E. *J. Chem. Phys.* **1985**, *83*, 5854.
(32) Klots, C. E. *Z. Phys. D: At., Mol. Clusters* **1987**, *5*, 83.
(33) Klots, C. E. *J. Phys. Chem.* **1988**, *92*, 5864.
(34) Weinheimer, C. J.; Lisy, J. M. *J. Chem. Phys.* **1996**, *105*, 2938.
(35) Cabarcos, O. M.; Weinheimer, C. J.; Martínez, T. J.; Lisy, J. M. *J. Chem. Phys.* **1999**, *110*, 9516.
(36) Cabarcos, O. M. An Experimental and Computational Study of Noncovalent Interactions in Gas-Phase Ion Solvation [Thesis]. Ph.D. Thesis, University of Illinois, 1998.
(37) Marcus, R. A. *J. Chem. Phys.* **1952**, *20*, 359.
(38) Herzberg, G., II *Infrared and Raman Spectra*; Van Nostrand Reinhold Company: New York, 1945.
(39) Guo, B. C.; Castelman, A. W., Jr. *Z. Phys. D: At. Mol. Clusters* **1991**, *19*, 397.
(40) Robinson, P. J.; Holbrook, K. A. *Unimolecular Reactions*; Wiley-Interscience: New York, 1972.
(41) Beyer, T.; Swinehart, D. F. *Commun. Assoc. Comput. Machin.* **1973**, *16*, 379.
(42) Stein, S. E.; Rabinovitch, B. S. *J. Chem. Phys.* **1973**, *58*, 2438.
(43) Khan, F. A.; Clemmer, D. E.; Schultz, R. H.; Armentrout, P. B. *J. Phys. Chem.* **1993**, *97*, 7978.
(44) Rodgers, M. T.; Ervin, K. M.; Armentrout, P. B. *J. Chem. Phys.* **1997**, *106*, 4499.
(45) Rodgers, M. T.; Armentrout, P. B. *J. Chem. Phys.* **1998**, *109*, 1787.
(46) Klots, C. E. *Z. Phys. D: At., Mol. Clusters* **1991**, *20*, 105.
(47) Weinheimer, C. J. The Role of Hydrogen Bonding in Alkali Metal Ion Solvation [Thesis]. Ph.D. Thesis, University of Illinois, 1998.
(48) Metropolis, N.; Ulam, S. *J. Am. Stat. Assoc.* **1949**, *44*, 335.
(49) Metropolis, N.; Rosenbluth, A. W.; Rosenbluth, M. N.; Teller, A. H.; Teller, E. *J. Chem. Phys.* **1953**, *21*, 1087.
(50) Allen, M. P.; Tildesley, D. J. *Computer Simulation of Liquids*; Oxford University Press: Oxford, 1987.
(51) Draves, J. A.; Luthey-Schulten, Z.; Liu, W.-L.; Lisy, J. M. *J. Chem. Phys.* **1990**, *93*, 4589.
(52) Caldwell, J. W.; Kollman, P. A. *J. Phys. Chem.* **1995**, *99*, 6208.
(53) Applequist, J.; Carl, J. R.; Fung, K.-K. *J. Am. Chem. Soc.* **1972**, *94*, 2952.
(54) Dang, L. X.; Rice, J. E.; Caldwell, J.; Kollman, P. A. *J. Am. Chem. Soc.* **1991**, *113*, 2481.
(55) Mó, O.; Yáñez, M.; Elguero, J. *J. Mol. Struct.* **1994**, *314*, 73.
(56) Curtiss, L. A.; Blander, M. *Chem. Rev.* **1988**, *88*, 827.
(57) Lovas, F. J.; Hartwig, H. *J. Mol. Spectrosc.* **1997**, *185*, 98.
(58) Guo, B. C.; Purnell, J. W.; Castleman, A. W., Jr. *Chem. Phys. Lett.* **1990**, *168*, 155.
(59) Coussan, S.; Bakkas, N.; Loutellier, A.; Perchard, J. P.; Racine, S. *Chem. Phys. Lett.* **1994**, *217*, 123.
(60) Huisken, F.; Kulcke, A.; Laush, C.; Lisy, J. M. *J. Chem. Phys.* **1991**, *95*, 3924.
(61) Huisken, F.; Kaloudis, M.; Kulcke, A. *J. Chem. Phys.* **1996**, *104*, 17.
(62) Fraley, P. E.; Rao, K. N. *J. Mol. Spectrosc.* **1969**, *29*, 348.
(63) Cho, C. H.; Singh, S.; Robinson, G. W. *J. Chem. Phys.* **1997**, *107*, 7979.
(64) Feller, D.; Glendening, E. D.; Woon, D. E.; Feyereisen, M. W. *J. Chem. Phys.* **1995**, *103*, 3526.
(65) Zwier, T. S. *Annu. Rev. Phys. Chem.* **1996**, *47*, 205.
(66) Curtiss, L. A.; Frurip, D. J.; Blander, M. *J. Chem. Phys.* **1979**, *71*, 2703.
(67) Lide, D. R. *CRC Handbook of Chemistry and Physics*, 78th ed.; CRC Press: New York, 1997.
(68) Weiner, S. J.; Kollman, P. A.; Nguyen, D. T.; Case, D. A. *J. Comput. Chem.* **1986**, *7*, 230.